Influence of polarization ellipticity on N_2^+ lasing in a strong laser field

Zoumingyang Zhu,[1] Shan Xue,[1,*] Yupeng Zhang,[1] Yuxuan Zhang,[1] Renjun Yang,[2,3] Shaohua Sun,[1] Zuoye Liu,[1] Pengji Ding,[1,†] and Bitao Hu[1]

[1]*School of Nuclear Science and Technology, Lanzhou University, Lanzhou 730000, China*
[2]*Institute of High Energy Physics, Chinese Academy of Sciences, Beijing 100049, China*
[3]*Spallation Neutron Source Science Center, Dongguan 523803, China*

(Received 17 March 2023; revised 14 June 2023; accepted 29 June 2023; published 18 July 2023)

A near-infrared femtosecond laser pulse produces laserlike coherent radiation from singly ionized N_2^+ molecules when it experiences filamentation in air or pure nitrogen, and the lasing radiation reaches maximal intensity when the driving pulse is slightly polarized elliptically. Based on a strong-field transient ionization model that considers ionization-induced quantum coherence, we reproduced the general feature of this counterintuitive dependence of the lasing intensity on pump laser ellipticity by numerically solving the Maxwell-Bloch equations of the lasing amplification process. The simulation results suggest that the competition effect between the increase of $B\,^2\Sigma_u^+ \leftarrow X\,^2\Sigma_u^+$ inversion probability and the decrease of overall N_2^+ ion production with the increasing ellipticity is mainly at the origin of observed ellipticity dependence. Additionally, the simulation predicts that ionization-induced quantum coherence also exhibits a nonzero ellipticity dependence and plays a nontrivial role in the weakly seeded and self-seeded scenarios. Our findings suggest that controlling the ionization-induced coherence could be a promising approach to improve the N_2^+ lasing generation.

DOI: 10.1103/PhysRevA.108.013111

I. INTRODUCTION

Lasing action from singly ionized nitrogen molecules (e.g., N_2^+ cations), produced by near-infrared femtosecond laser pulses in subatmospheric nitrogen gas as it experiences filamentation, has attracted great interest in the research communities of ultrafast nonlinear optics and strong-laser-field physics in last decade [1–13]. Optical amplifications at wavelengths of 391 and 428 nm occur for transitions between the second excited state $B\,^2\Sigma_u^+$ and the ground state $X\,^2\Sigma_u^+$ of N_2^+ ions [see Fig. 1(a)], resulting in lasing emission in self-seeding or external-resonant-seeding regimes. The research on N_2^+ lasing is mainly driven by potential applications in remote atmospheric sensing due to its laserlike characteristics on the one hand and a better understanding of its gain mechanism on the other hand. So far, severe challenges remain in both aspects. For applications, the strong quenching effect of the oxygen molecules prevents backward-propagating N_2^+ lasing generation in ambient air, though amplification of a resonant seeding pulse has been observed in the backward direction [14]. In the aspect of exploring the underlying physics, the combination of strong-field ionization, electronic-vibrational-rotational excitation, nonlinear propagation, and quantum coherence brings tremendous difficulties in fully understanding the gain mechanism for N_2^+ lasing. Few theories, including three-state postionization coupling [3,5], transient rotational population inversion [15,16], and lasing without inversion [11,17,18], have been proposed to explain the origin of optical gain in N_2^+ ions. It is currently under hot debate whether population inversion exists in the lasing process. Meanwhile, several critical experimental observations of N_2^+ lasing, such as pulse-duration-dependent periodic variation of the lasing intensity with the pump laser wavelength [6], complicated polarization evolution of the externally seeded lasing signal reacting to the polarization status change of the seeding pulse [19], temporally delayed superradiance nature in an external-seeding scheme [4,20], and abnormal dependence of the lasing intensity on the polarization ellipticity of the driving laser pulse [4,7,21–23], have not been well explained in the frameworks of current models. Among the abovementioned observations, the unexpected dependence of N_2^+ lasing on pump laser ellipticity is particularly intriguing since several factors that determine the lasing generation, such as ionization probability, population redistribution among related electronic states, and coherence, will vary accordingly and interplay when changing the pump laser ellipticity. It was experimentally observed that the N_2^+ lasing signal increases when rotating the quarter-wave plate (QWP) slightly off the angle of linear polarization, e.g., an elliptically polarized pump laser pulse produces the strongest lasing signal with optimal ellipticity ε in the range of 0.15–0.40, depending on the specific experimental conditions [21,22,24] [see Figs. 1(b) and 1(c)]. As a strong contrast, side fluorescence from N_2^+ ions at the same wavelength exhibits a monotonical decrease as ε increases, an expected behavior from strong-field ionization theory. Recently, Fu *et al.* used multiple-order QWP to modulate the polarization state of the pump laser pulse and observed a similar ellipticity dependence of a 391-nm lasing signal, but this was not observed for 428-nm lasing [23]. A qualitative understanding of the nonzero ellipticity

*xues@lzu.edu.cn
†dingpj@lzu.edu.cn

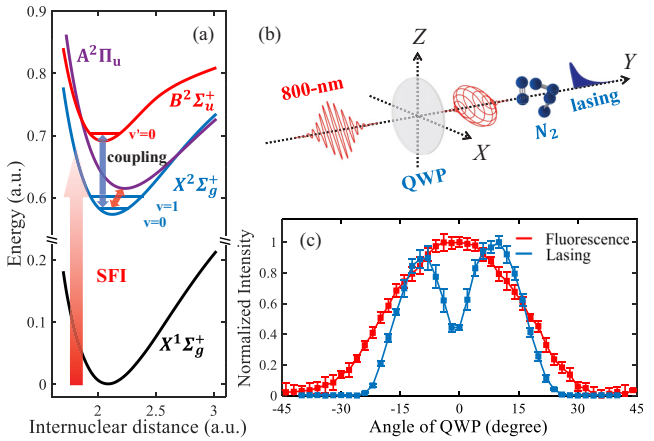

FIG. 1. (a) Schematic of relevant energy levels of nitrogen molecules. N_2^+ lasing at wavelengths of 391 and 428 nm corresponds to the $B\,^2\Sigma_u^+(v=0) \rightarrow X\,^2\Sigma_u^+(v'=0,1)$ transitions, respectively. SFI stands for the strong-field ionization process. (b) Optical setup to generate N_2^+ lasing emission with an elliptical polarized 800-nm femtosecond laser pulse. (c) 391-nm lasing and fluorescence signal as a function of the rotational angle of QWP, in which an obvious "dip" structure around the linear polarization is shown for the lasing signal.

dependence of N_2^+ lasing was provided in the framework of a postionization three-state coupling model.

As far as we know, the angle dependence effect has not been considered in the study of ellipticity dependence of N_2^+ lasing. This weakens the credibility of the explanations because initially the molecular orientations are isotropic. More importantly, strong-field ionization of molecules with multicycle femtosecond pulses can prepare a certain degree of coherence among electronic states of ionized molecules, which has been so far ignored in the theoretical treatment of N_2^+ lasing. To more accurately understand the abnormal ellipticity dependence of N_2^+ lasing signal, the influence of Euler angles on population inversion, coherence, and final lasing signals should be investigated. In this work, we perform experimental and theoretical studies to further investigate this phenomenon because gaining comprehensive knowledge of its physical origin is essential to determine the self-contained gain mechanism of N_2^+ lasing. A strong-field transient ionization model is adopted to calculate the generated reduced density matrix of N_2^+, i.e., populations and coherences, for all angles of the molecular axis with respect to the laser field polarization. Numerical simulation based on solving Maxwell-Bloch equations well reproduces the typical observations of abnormal dependence of N_2^+ lasing intensity on the pump laser ellipticity.

II. EXPERIMENTAL METHODS AND RESULTS

We performed the experiments with a commercial Ti:sapphire laser system (Astrella, Coherent Inc.) which provides 800-nm, 35-fs, ~7-mJ laser pulses at a repetition rate of 1 kHz. The experimental setup is schematically illustrated in Fig. 2. The laser beam is split by a beam splitter (BS, R90/T10) into two arms: One arm with a pulse energy of ~500 μJ serves as the seed beam, while another one with the most pulse energy serves as the pump beam. We employed external seed in this study to exclude any uncertain influence of a self-generated seed from continuum generation and second harmonic generation, since these two nonlinear effects decrease as the ellipticity of the femtosecond laser pulse increases. In the seed beam, the laser frequency was first doubled by a 0.1-mm-thick β-barium borate crystal. By rotating the crystal in the plane parallel to the optical table, the phase-matched angle of the crystal can be optimized and the seed pulse that covers the lasing wavelength at 391 or 428 nm can be generated. The pulse energy of the 391-nm seed light before passing through the lens in front of the chamber is ~0.3 μJ (4 orders of magnitude lower than the pump pulse energy). We estimate the intensity of the seed light in the plasma filament to be around ~10^9 W/cm^2, and it could be slightly lower in the case of the 428-nm seed. The linearly polarized pump beam first passes through a zero-order QWP (central wavelength at 808 nm). It needs to be emphasized here that the polarization ellipticity of the 800-nm pump laser pulse was critically determined by measuring its polarization status before and after the focus using polarizers, which suggests that the pump laser cannot reach a perfect circular polarization

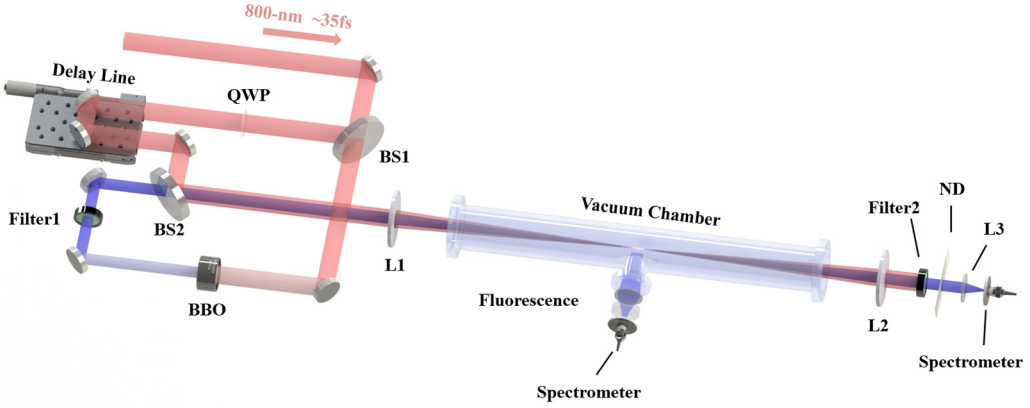

FIG. 2. Schematic illustration of the experimental setup. BS, beam splitter; QWP, quarter wave-plate; BBO, β-barium borate; DM, dichroic mirror; ND, neutral density filter.

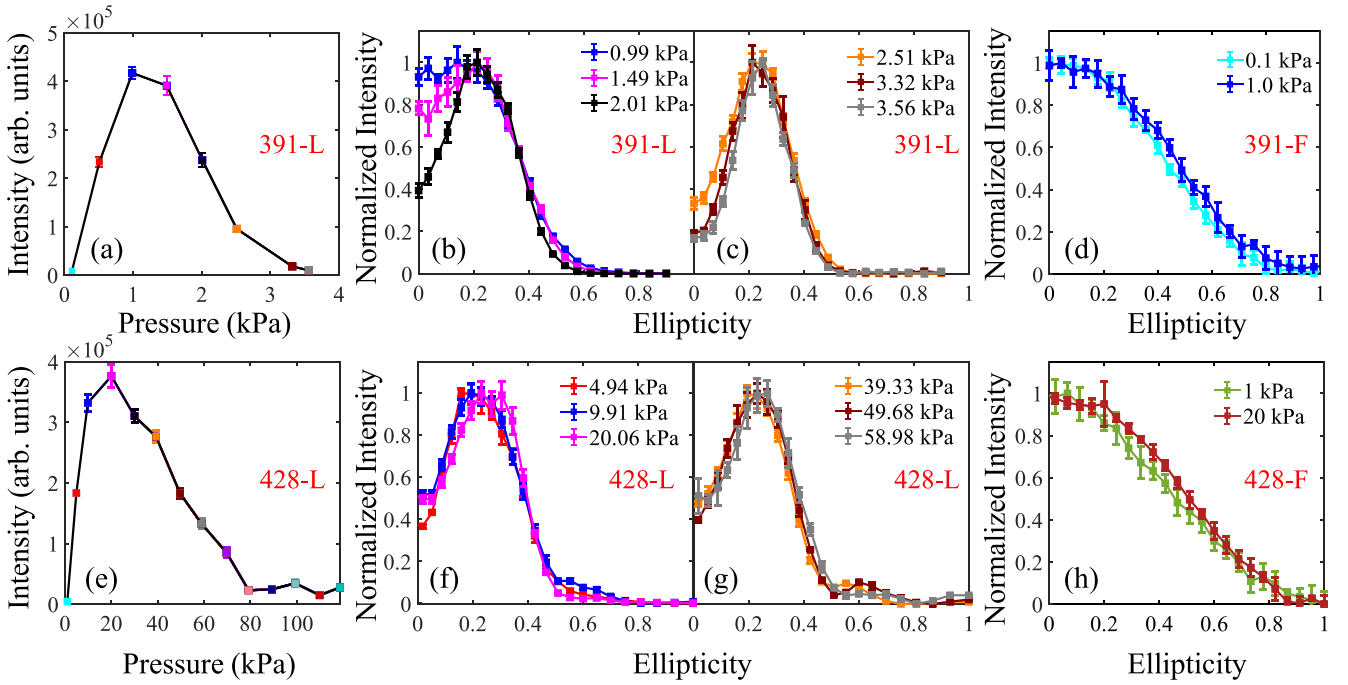

FIG. 3. (a) The peak intensity of the 391-nm lasing pulse as a function of the nitrogen gas pressure. Each data point was obtained by averaging 100 laser shots at a pump ellipticity of 0.2. (b) and (c) Normalized 391-nm lasing signal as a function of the pumping laser ellipticity for varying gas pressure from 0.99 to 3.56 kPa. The color of each curve is consistent with that of the data point in panel (a). Each data point was averaged for 100 laser shots. (d) Side 391-nm fluorescence intensity as a function of the pumping laser ellipticity for three typical nitrogen gas pressures. Each data point was averaged for 100 laser shots. The results of 428-nm lasing were presented in panels (e)–(h) correspondingly. The labels represent the results of 391-nm lasing (391-L), 391-nm fluorescence (391-F), 428-nm lasing (428-L), and 428-nm fluorescence (428-F).

because its polarization varies as it experiences focusing and filamentation [25]. A delay line, composed of a motorized translation stage and two highly reflective mirrors, was placed in the pump beam, which provides a temporal resolution of ∼52 fs. A dichroic mirror (DM, R800/T400) was used to combine the pump and seed beams, which were then focused together by a convex spherical lens (L1, focal length ∼500 mm) into a gas chamber filled with pure nitrogen gas.

Forward N_2^+ lasing emissions were collected by another convex spherical lens (L2, focal length of 150 mm) into a high-resolution spectrometer (McPherson 2061, resolution of ∼0.01 nm) through a fiber. Neutral density filters were used to attenuate the emission intensity, and specific bandwidth filters ($390 \pm 10/430 \pm 10$ nm) were used to select the lasing signals. Side fluorescence of N_2^+ ions from the interacting volume was also collected using a telescope consisting of two lenses ($f = 200$ and 100 mm) into the spectrometer.

The upper panels in Fig. 3 show the results of 391-nm lasing, for which we first investigated its intensity dependence on the pressure [see Fig. 3(a)]. The measurements were performed with a pump laser pulse energy of ∼2.4 mJ. The maximal lasing signal was detected at a pressure of approximately 1 kPa. For different pressures, the ellipticity dependencies of the 391-nm lasing intensity were then measured correspondingly, as shown in Figs. 3(b) and 3(c). The important observation from the results is that maximal lasing generation occurs as the pump laser polarization is rotated to be slightly elliptical, e.g., $\varepsilon \sim 0.2$. As distinct from the lasing behavior, the 391-nm fluorescence of N_2^+ ions measured in the transverse direction monotonously decreases when ε increases, as displayed in Fig. 3(d). The fluorescence behavior can be readily understood as a result of the reduced yield of N_2^+ ions because strong-field ionization theory predicts that the ionization probability of molecules is fully determined by the instantaneous electric field, which simply decreases as the laser ellipticity increases [26].

Furthermore, this abnormal ε-dependence of the N_2^+ lasing signal becomes more significant as the pressure increases from 0.99 to 3.56 kPa. Our results show the most profound abnormality of the ε-dependence curve compared to the reported experiments in Refs. [21–24]. The lasing signal for $\varepsilon = 0$ (linear polarization), normalized to that of optimal laser ellipticity, can be as small as ∼0.2. Similar results were reported using a 10th-order QWP to manipulate the pump laser polarization [23]. It should be mentioned that the lasing signal shown in Fig. 2 was integrated over both P and R branches of the lasing emission spectrum. We also separately processed the lasing signals in two branches for varying pump laser ellipticity and obtained results similar to those of Fig. 3.

For 428-nm lasing, we performed similar experiments and the results are shown in the lower panels of Fig. 3. Similar features can be noticed, except that the ellipticity dependence curves of 428-nm lasing intensity for different pressures are almost the same. The normalized lasing signal for $\varepsilon = 0$ stays around 0.4–0.5 for varying pressures in the whole range of

428-nm lasing generation. The difference of ε-dependence curve profiles between two lasing signals should relate to the fact that 391-nm lasing was generated under quite low pressures, whereas 428-nm lasing was generated under high pressures and also in a much broader pressure range. Thus, a comprehensive observation for both lasings is that the ε-dependence profile becomes more significant as the pressure increases in the low-pressure regime, and the profile significance remains unchanged as the pressure exceeds ~5.0 kPa. The change of gas pressure mainly affects the continuum generation, second harmonic generation, and pump laser intensity in the interaction region. In our measurements, a strong external seeding pulse was intentionally used to exclude potential influence from second harmonic generation and continuum generation. Therefore, the change of pump laser intensity with the increase of gas pressure might dictate different behaviors of ε-dependence curves of 391- and 428-nm lasing. Further investigations on how does the laser intensity change at low pressures prior to the laser filamentation regime as well as on the influence of intensity clamping effect at high pressures would be required.

III. THEORETICAL MODEL

To understand the abnormal dependence of N_2^+ lasing on pump laser ellipticity, we adopt the strong-field transient ionization (SFTI) model developed in Refs. [27,28] to calculate the reduced density matrix (DM) of N_2^+ ions after the pump laser pulse, and then we perform simulations on the ellipticity dependence of both 391- and 428-nm lasing signals via numerically solving the Maxwell-Bloch equations. The validity of the SFTI model has been verified on a one-dimensional H_2^+ system [27]. In this work, this model is described in the form of optical Bloch equations.

For a molecular system interacting with strong laser fields within tens of femtoseconds, the DM can be expressed in terms of the electronic-vibrational (vibronic) states v_i^m (ith vibrational state on the mth potential energy curve) under the Born-Oppenheimer approximation, $\rho_{ij}^{mn} = \langle \psi_m \chi_i^m | \hat{\rho} | \psi_n \chi_j^n \rangle$. Here, χ_i^m is the wave function of state v_i^m, and ψ_m denotes the wave function of the mth electronic state. For the N_2^+ system concerned, $m, n = x, a, b$, where x, a, and b represent states $X\,^2\Sigma_u^+$, $A_2\Pi_u$, and $B\,^2\Sigma_u^+$, respectively. Then the optical Bloch equations read

$$i\frac{\partial}{\partial t}\rho_{ij}^{mn} = \omega_{ij}^{mn}\rho_{ij}^{mn} + i\Gamma_{ij}^{mn} - \boldsymbol{\mathcal{E}}^{(M)} \cdot \sum_{o,l} \left(\mathbf{u}_{il}^{mo}\rho_{lj}^{on} - \rho_{il}^{mo}\mathbf{u}_{lj}^{on}\right), \tag{1}$$

where $\omega_{ij}^{mn} = E_i^m - E_j^n$ is the energy difference between two states with $E_{i(j)}^{m(n)}$ being the eigenenergy of state $v_{i(j)}^{m(n)}$. $\mathbf{u}_{ij}^{mn} = \langle \chi_i^m | \mathbf{u}_{mn}(R) | \chi_j^n \rangle$ is the vibronic-state transition dipole moment element with $\mathbf{u}_{mn}(R)$ being the R-dependent electronic-state transition dipole moment element between states m and n. $\boldsymbol{\mathcal{E}}^{(M)}$ is the pump electric field defined in the molecule-fixed xyz coordinate system, which can be transformed from the electric field in the space-fixed (SF) XYZ coordinate system $\boldsymbol{\mathcal{E}}^{(S)}$ by $\boldsymbol{\mathcal{E}}^{(M)} = \mathbf{R}(\alpha\beta\gamma)\boldsymbol{\mathcal{E}}^{(S)}$ [29]. Here, α, β, and γ are the Euler angles in the zyz convention (see Fig. 4). $\mathbf{R}(\alpha\beta\gamma)$ is the rotational matrix and reads

$$\mathbf{R}(\alpha\beta\gamma) = \begin{bmatrix} \cos\gamma\cos\beta\cos\alpha - \sin\gamma\sin\alpha & -\cos\gamma\cos\beta\sin\alpha - \sin\gamma\cos\alpha & \cos\gamma\sin\beta \\ \sin\gamma\cos\beta\cos\alpha + \cos\gamma\sin\alpha & -\sin\gamma\cos\beta\sin\alpha + \cos\gamma\cos\alpha & \sin\gamma\sin\beta \\ -\sin\beta\cos\alpha & \sin\beta\sin\alpha & \cos\beta \end{bmatrix}. \tag{2}$$

The elliptically polarized pump electric field $\boldsymbol{\mathcal{E}}^{(S)}$ in the ZX plane can be expressed as

$$\begin{aligned} &\boldsymbol{\mathcal{E}}^{(S)}(\theta, t) \\ &= \boldsymbol{\mathcal{E}}_Z^{(S)}(t) + \boldsymbol{\mathcal{E}}_X^{(S)}(t) \\ &= E_0\cos(\theta) f\left(t - \frac{T_d}{2}\right)\mathbf{e}_Z^{(S)} + E_0\sin(\theta) f\left(t + \frac{T_d}{2}\right)\mathbf{e}_X^{(S)}. \end{aligned} \tag{3}$$

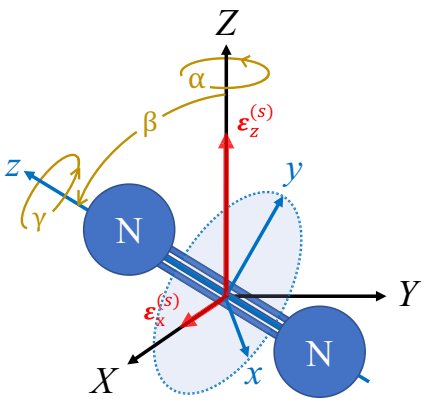

FIG. 4. The Euler angles and pump field components. The Eular angles are defined in the zyz convention. The molecular-fixed xyz coordinate system is obtained by sequentially rotating the system from the space-fixed (SF) XYZ coordinate system by an angle α around the Z axis, followed by an angle β around the current y axis, and finally an angle γ around the new z axis. The red thick arrows represent the electric field components defined in the SF coordinate system.

Here, θ denotes the angle between the polarization direction of the linearly polarized pump laser pulse and the fast axis of QWP, E_0 is the field amplitude, and $T_d = (1/4)(2\pi/\omega)$ is the delay time induced by the zero-order QWP. $f(t) = \exp[-2ln2(t^2/\tau^2)]\sin(\omega t)$ represents the laser field envelope in which τ and ω denote the full width at half maximum of the duration and the carrier frequency, respectively. The ellipticity of the pump laser is then defined as $\varepsilon = \tan\theta$.

The key part of the SFTI model is reflected in the second term in Eq. (1). It represents the transient DM elements injected at each instant, which reads

$$\Gamma_{ij}^{mn}(t) = \sqrt{\Gamma_i(\boldsymbol{\mathcal{E}}^{(M)}(t))}c_i^{m(FC)}\sqrt{\Gamma_j(\boldsymbol{\mathcal{E}}^{(M)}(t))}c_j^{n(FC)} \times n_{N_2}(t)\prod_{\xi=x,y,z}\mathrm{sgn}\left[\mathcal{E}_\xi^{(M)}(t)\right]^{(2-P_\xi^m-P_\xi^n)/2}. \quad (4)$$

Here, Γ_i is the transient ionization rate from the neutral to the ith electronic state of N_2^+ at time t, which is calculated by the molecular Ammosov-Delone-Krainov theory. $c_i^{m(\mathrm{FC})}$ is the square root of the Franck-Condon factor of state v_i^m, i.e., $\langle v_i^m|v_0^{(\mathrm{neutral})}\rangle$, where $v_0^{(\mathrm{neutral})}$ represents the vibrational ground state of the neutral. $n_{N_2}(t)$ accounts for the remaining population probability of the neutral N_2 molecule at time t. The last term in Eq. (4) describes the parity effect of ionization orbitals, which plays a crucial role in the accumulation of the ionic coherences within the duration of the driving laser pulse [27,30]. P_ξ^m describes the reflection symmetry of the ionization orbital (generating the mth electronic state of N_2^+) with respect to the plane perpendicular to the ξth axis, with a value of ±1 representing the $\pm$ symmetry.

It should be emphasized that the value of Eq. (4) depends on the electric field direction and also the molecular axis. In other words, the effect of geometric alignment of the ionization-produced N_2^+ ensemble has been taken into consideration in the SFTI model. However, we assume that the dynamic alignment effects of the neutral molecule and molecular ion are negligible. This assumption is based on the fact that the pump-molecule interaction time is on a timescale of tens of femtoseconds, which is much shorter than the ~8-ps rotational revival period. Importantly, this SFTI model takes the ionization-induced coherence (i.e., coherence injection) into consideration, which was assumed as zero in previous models [31–35]. We found that the ionization-induced coherence has a nonzero value and also plays a non-negligible effect in weakly seeded or self-seeded N_2^+ lasing scenarios. Moreover, by solving the time-dependent Schrödinger equation repeatedly starting from every ionization instant, followed by adding up the final DMs at the end of the laser pulse, the accumulated mixed-state DM is numerically identical to the one obtained by solving the optical Bloch equation of Eq. (1). The advantage of solving Eq. (1) is that it is extremely computationally efficient.

After obtaining the ionic DM generated by the pump laser pulse, subsequent lasing amplification can be simulated by propagating the Maxwell-Bloch (MB) equations [11,17,36]. Considering three ionic vibronic states (v_0^x, v_1^x, and v_0^b) interacting with the lasing field propagating along $\mathbf{e}_Y^{(S)}$, the MB equations in the retarded frame ($t' = t - Y/c$) read as follows:

$$\frac{\partial\tilde{E}_{i0}^{xb}}{\partial Y} = \frac{i\omega_{i0}^{xb}u_{i0}^{xb}N_{\mathrm{ion}}}{\epsilon_0 c}\tilde{\rho}_{i0}^{xb*}\cos\beta, \quad (5)$$

$$\frac{\partial\tilde{\rho}_{ij}^{xx}}{\partial t'} = \left[iu_{i0}^{xb}\tilde{\rho}_{j0}^{xb*}e^{i\omega_{i0}^{xb}t} - iu_{j0}^{xb}\tilde{\rho}_{i0}^{xb}e^{-i\omega_{j0}^{xb}t}\right] \times E^{xb}\cos\beta - \gamma_d\tilde{\rho}_{ij}^{xx}, \quad (6)$$

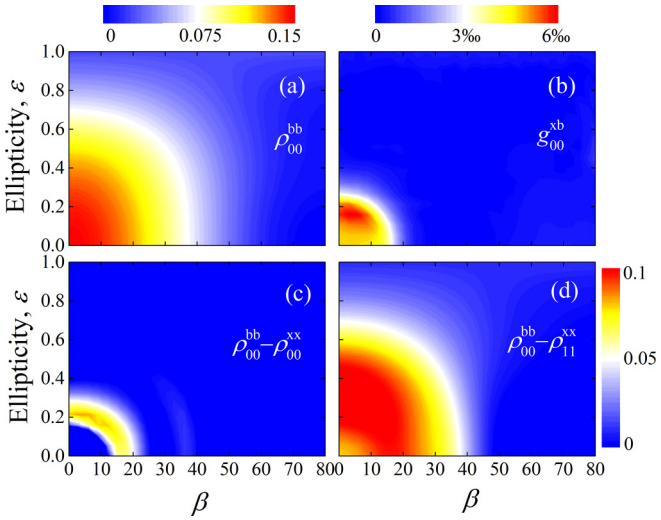

FIG. 5. Density matrix elements and degree of coherence as a function of β and ellipticity calculated by the strong-field transient ionization model. (a) Population of state v_0^b. (b) Degree of coherence between states v_0^x and v_0^b. Population inversion of (c) $v_0^x - v_0^b$ and (d) $v_1^x - v_0^b$, respectively. Panels (c) and (d) share the same color scale.

$$\frac{\partial\tilde{\rho}_{00}^{bb}}{\partial t'} = 2\mathrm{Im}\left\{\sum_i iu_{i0}^{xb}\rho_{i0}^{xb}E^{xb}\cos\beta\right\}, \quad (7)$$

$$\frac{\partial\tilde{\rho}_{i0}^{xb}}{\partial t'} = \left[iu_{i0}^{xb}\rho_{00}^{bb}e^{i\omega_{i0}^{xb}t} - \sum_j iu_{j0}^{xb}\tilde{\rho}_{ij}^{xx}e^{i\omega_{j0}^{xb}t}\right] \times E^{xb}\cos\beta - \gamma_d\tilde{\rho}_{i0}^{xb}. \quad (8)$$

Here, $i, j = 0, 1$. $\tilde{\rho}_{ij}^{mn} = \rho_{ij}^{mn}e^{i\omega_{ij}^{mn}t}$ is the slow-varying DM element. N_{ion} is the density of N_2^+ ions. ϵ_0 is the vacuum permittivity. c is the speed of light. γ_d describes the dephasing rate of coherence. The lasing field reads $E^{xb} = \sum_i(\frac{1}{2}\tilde{E}_{i0}^{xb}e^{i\omega_{i0}^{xb}t} + \mathrm{c.c.})$.

IV. SIMULATION RESULTS AND DISCUSSION

In the simulations, vibronic states $v_0^x \sim v_7^x$, $v_0^a \sim v_7^a$, and $v_0^b \sim v_7^b$ are considered in Eq. (1). The pump laser pulse is set to 40 fs with an intensity of 3×10^{14} W/cm^2. The reduced DMs of N_2^+ are calculated for different molecular orientations with varying ellipticities. It is found that the Euler angles α and γ mainly affect the population distributions of the two degenerate states $A\,^2\Pi_{ux}$ and $A\,^2\Pi_{uy}$ but have negligible influence on the final $X\,^2\Sigma_g^+$-$B\,^2\Sigma_u^+$ DM elements. In the following, we only focus on the influence of the Euler angle β, which is the angle between the molecular axis and $\mathbf{e}_Z^{(S)}$ in the polarization plane of the pump field.

We first explain the normal ellipticity dependence of the side fluorescence in the experiment. Figure 5(a) shows the calculated DM element ρ_{00}^{bb} versus β and the pump laser ellipticity ε. It can be seen that ρ_{00}^{bb} are always maximum at $\varepsilon = 0$ for all angles and then decrease as ε increases. Since the fluorescence signal is proportional to the population of v_0^b that is quantified by ρ_{00}^{bb}, this simulation result well explains

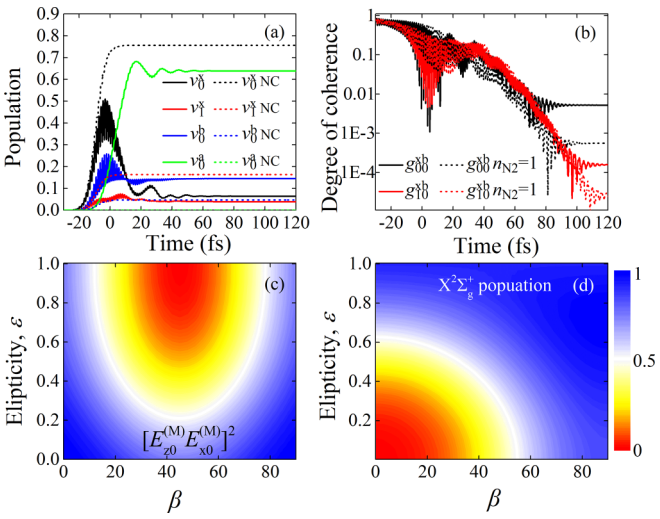

FIG. 6. (a) Time-dependent ionic state populations during the duration of the pump pulse for $\beta = 0^\circ$ and $\varepsilon = 0.2$. Those without considering the dipole coupling effect are shown by the dashed lines, marked with NC. (b) Same as panel (a), but for the time-dependent degree of coherences. Results calculated with $n_{N_2} = 1$ are shown by the dashed lines. (c) Normalized $[E_{z0}^{(M)} E_{x0}^{(M)}]^2$ as a function of β and ε. (d) Normalized $X\,^2\Sigma_g^+$-state population without considering the dipole coupling effect as a function of β and ε.

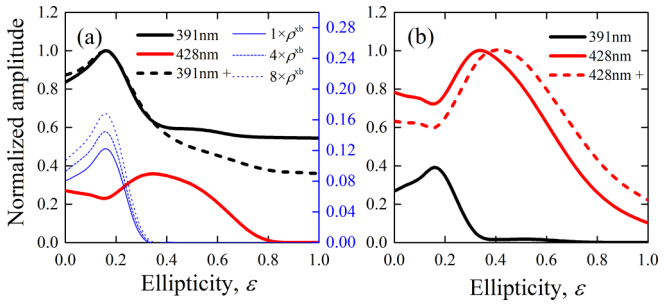

FIG. 7. (a) Normalized lasing signal as a function of the pump laser ellipticity, under the conditions of a 391-nm seed pulse and a 0.6-kPa gas pressure. The 391-nm lasing signals with weak seed are calculated under three conditions: $1\times\rho_{00}^{xb}$, $4\times\rho_{00}^{xb}$, and $8\times\rho_{00}^{xb}$. (b) Same as panel (a), but for a 428-nm seed pulse with a pressure of 60 kPa. Signals calculated with 35-fs, 3.5×10^{14} W/cm^2 pump pulses are shown by thick dashed lines, denoted by the "+" symbol.

the monotonous decrease of the side fluorescence with the increasing ellipticity shown in Figs. 3(d) and 3(h).

For the lasing signal, its intensity is closely related to the population inversion between relevant states. Therefore, ρ_{00}^{bb}–ρ_{00}^{xx} (generating 391-nm lasing) and ρ_{00}^{bb}–ρ_{11}^{xx} (generating 428-nm lasing) at different β and ε are respectively calculated and displayed in Figs. 5(c) and 5(d). It can be seen that both of the two quantities exhibit dips at linear polarization for small angles. In general, the peaks of population inversion locate within $\varepsilon = 0.1$–0.3 for the 391-nm case and $\varepsilon = 0.2$–0.5 for the 428-nm case when $\beta < 15^\circ$.

Another factor that may influence lasing generation is quantum coherence. Calculations of the SFTI model indicate that the degree of coherences (DOCs) $g_{ij}^{xb} = |\rho_{ij}^{xb}|/\sqrt{\rho_{ii}^{xx}\rho_{jj}^{bb}}$ of state pairs $v_1^x - v_0^b$ and $v_0^x - v_0^b$ are both very weak at the end of the pump laser pulse. Figure 5(b) shows g_{00}^{xb} versus β and ε. Clearly g_{00}^{xb} peaks at nonzero ellipticity for all β, and its maximum is only ~0.6‰. g_{10}^{xb} is even much weaker than g_{00}^{xb} [as shown in Fig. 6(b)] and is not depicted here. The reason for the small coherence is that the parities of the ionization orbitals HOMO and HOMO-2 that respectively produce $X\,^2\Sigma_g^+$ and $B\,^2\Sigma_u^+$ states are opposite. Because $\omega_{00(01)}^{bx} \approx 2\omega$, the transient DM elements populated at one field crest $\rho_{00(10)}^{xb(\mathrm{tran})}(t_1)$ and the adjacent field crest $\rho_{00(10)}^{xb(\mathrm{tran})}(t_1 + \pi/\omega)$ will interfere destructively at the end of the pump pulse, resulting in a small value of $\rho_{00(10)}^{xb}$. However, as discussed below in Fig. 7(a), even such weak coherence can exert non-negligible effects on the lasing amplification in a weakly seeded scenario. To better understand the underlying mechanisms in the generation of the population inversion and coherence during the pump laser pulse, the case of $\beta = 0^\circ$ and $\varepsilon = 0.2$ is taken as an example for detailed analysis. Figure 6(a) shows the population evolution of states v_0^x, v_1^x, v_0^b, and v_0^a during the pump laser pulse. The dashed lines are those populations without considering the dipole coupling effect, i.e., the third term in Eq. (1). By comparison, one can see that the populations of v_0^x and v_1^x decrease, but those of v_0^b and v_0^a increase when the coupling effect is included. Especially, considerable population transfer from $X\,^2\Sigma_g^+$ to $A\,^2\Pi_u$ is caused by the single-photon resonance. This is consistent with the findings of previous models [3,5], where the $A\,^2\Pi_u$ state serves as a "population reservoir." As a result, the population inversion between $v_{0(1)}^x$ and v_0^b builds up at the end of the pump laser pulse.

The time-dependent DOCs of state pairs v_0^x-v_0^b and v_1^x-v_0^b are shown in Fig. 6(b). It can be seen that both g_{00}^{xb} and g_{10}^{xb} evolve to smaller values as time increases because of the opposite parities of neutral HOMO and HOMO-2. However, at the end of the pump laser pulse, g_{00}^{xb} still has a non-negligible value. This is mainly due to the evolution of $n_{N_2}(t)$ in Eq. (4), which disrupts the balance of the destructive interference of periodically injected coherences at each field crest. Therefore, some coherence remains at the end of the pump laser pulse. For comparison, the DOCs calculated for constant density of neutral nitrogen molecule with $n_{N_2} \equiv 1$ are depicted in Fig. 6(b) as dashed lines. In this case, both g_{00}^{xb} and g_{10}^{xb} become 1 order of magnitude smaller.

Based on the above analysis, we know that the probability of the population inversion depends on the excitation from $X\,^2\Sigma_g^+$ to $B\,^2\Sigma_u^+$ and the pumping from $X\,^2\Sigma_g^+$ to $A\,^2\Pi_u$. The strengths of these two processes are proportional to the squares of the field components' amplitudes, $E_{z0}^{(M)2}$ and $E_{x0}^{(M)2}$. For this reason, we plot $[E_{z0}^{(M)} E_{x0}^{(M)}]^2$ versus β and ε in Fig. 6(c) to demonstrate the probability of population inversion. With the increase of ε, the inversion probability increases. On the other hand, the absolute value of population inversion is directly related to the $X\,^2\Sigma_g^+$-state population generated by the strong-field ionization. Figure 6(d) shows the $X\,^2\Sigma_g^+$-state population at the end of the pump pulse without considering the coupling term in Eq. (1). One can see that the populations are larger at smaller ellipticities and angles. As a result, the combined effect of $[E_{z0}^{(M)} E_{x0}^{(M)}]^2$ and the $X\,^2\Sigma_g^+$-state population leads to the bump of the population inversion

along ε, and the inversion mostly occurs at small angles. This readily explains the results shown in Figs. 5(c) and 5(d). To compare with the experimental results, both lasing signals are calculated by propagating Eqs. (5)–(8). The injected seed pulse is polarized along $\mathbf{e}_z^{(S)}$. Its intensity is set to be 4 orders of magnitude lower than the pump laser intensity. The gas pressure is 0.6 kPa for the 391-nm lasing and 60 kPa for the 428-nm lasing. Other parameters are set as follows: 3-mm medium length and $\gamma_d = 2.5\ \mathrm{ps}^{-1}$. The lasing intensity is obtained by Fourier transformation of the electric field followed by integrating over β, i.e.,

$$I_{i0}^{xb} \propto \left\{ \iint_{\omega_{0i}^{bx}-0.005}^{\omega_{0i}^{bx}+0.005} E^{xb}(\omega,\beta) 2\pi \sin\beta d\omega d\beta \right\}^2, \qquad (9)$$

where $i = 0$ and 1. Figures 7(a) and 7(b) show the normalized lasing signals (thick solid lines) versus ellipticity for the 391-nm and 428-nm seeding cases, respectively. In the case of 391-nm seeding and low pressure, the 391-nm lasing signal dominates and reaches its maximum at $\varepsilon \approx 0.18$. For 428-nm seeding and high pressure, the 428-nm lasing signal dominates, and the maximum is located around $\varepsilon \approx 0.33$. The simulated results qualitatively reproduce the anomalous dependence of the lasing signals on pump laser ellipticity observed in the experiments. Relatively larger ellipticity for maximal 428-nm lasing intensity can be more clearly observed in Ref. [22]. To demonstrate the universality of the ellipticity dependence, lasing signals (thick dashed lines) calculated with 35-fs, 3.5×10^{14} W/cm^2 pump pulses are also depicted in Fig. 7. The anomalous trend still exists. Interestingly, the lasing intensity remains nearly unchanged regardless of whether or not the ionization-induced coherence is taken into account as the initial condition when solving Eqs. (5)–(8). This is because such coherence is significantly weaker compared to the coherence generated by the dipole coupling between $X\,^2\Sigma_g^+$ and $B\,^2\Sigma_u^+$ induced by the seed pulse. However, if the seed pulse is weak, for instance, in the self-seeded scenario, the influence of the ionization-induced coherence will become more noticeable. To illustrate this point, two artificial ionization-induced coherences are considered as the initial conditions: $4\times\rho_{00}^{xb}$ and $8\times\rho_{00}^{xb}$. A seed pulse with an intensity of 1.5×10^6 W/cm^2 is adopted to mimic the weak seed. The calculated results are shown as blue thin lines (right, y axis) in Fig. 7(a). As can be seen, the anomalous ellipticity dependence still exists. As the coherence increases, the lasing intensity gradually increases. Therefore, we conclude that both the seed pulse and the ionization-induced coherence contribute positively to the lasing amplification. The seed-produced or the ionization-induced coherence (i.e., polarization amplitude) will be gradually amplified as the lasing electric field propagates through the filament, leading to the lasing amplification. It should be pointed out that population inversion is still the main cause of the lasing gain. Optimizing the interstate coherence could be a potential way to improve the lasing signal.

Note that, with a pump laser intensity of $\sim10^{14}$ W/cm^2, the electron recollision effect is worthy of being considered theoretically when the pump ellipticity is small, although its role may not be as important as laser coupling [7,37]. Such an effect will not only enlarge the population inversion but also modify the interstate coherence, affecting the coupling dynamics during interaction of the pump pulse and N_2^+ [4,6]. In addition, the population redistribution of rotational states on the vibronic states (v_0^x, v_1^x, and v_0^b) could promote the population inversion of some rotational-state pairs [38]. Those factors could relax the intensity requirement so that a lower pump laser intensity could initiate the lasing generation. We will investigate these mechanisms systematically based on the SFTI model in further works.

V. CONCLUSION

In conclusion, we have experimentally investigated the abnormal ellipticity dependence of N_2^+ lasing in subatmospheric nitrogen irradiated with intense 800-nm femtosecond laser pulses and theoretically reproduced such observations by performing Maxwell-Bloch simulations based on the SFTI model. In the strongly seeded scenario, the combined effect of two factors, i.e., the increase of population inversion between $X\,^2\Sigma_g^+$ and $B\,^2\Sigma_u^+$ due to efficient population transfer from $X\,^2\Sigma_g^+$ to $A\,^2\Pi_u$ and the decrease of $X\,^2\Sigma_g^+$ state population when the pump laser ellipticity changes from 0 to 1, results in the abnormal dependence of N_2^+ lasing signal on ellipticity. Quantum coherence between $X\,^2\Sigma_g^+$ and $B\,^2\Sigma_u^+$ begins to take effect in the weakly seeded and self-seeded scenarios, which additionally contributes to the abnormal ellipticity dependence. Although the strong-field ionization-induced coherence has a limited effect on the lasing signal, optimizing the degree of coherence may be an effective way to improve the N_2^+ lasing generation.

ACKNOWLEDGMENTS

This research work is supported by the National Science Foundation for Young Scientists of China (Grants No. 12004147, No. 11904146, No. 12027809, and No. U1932133) and the open project of the Shanghai Institute of Optics and Fine Mechanics (SIOM), Chinese Academy of Sciences.

[1] J. Yao, B. Zeng, H. Xu, G. Li, W. Chu, J. Ni, H. Zhang, S. L. Chin, Y. Cheng, and Z. Xu, Phys. Rev. A **84**, 051802(R) (2011).

[2] H. Zhang, C. Jing, J. Yao, G. Li, B. Zeng, W. Chu, J. Ni, H. Xie, H. Xu, S. L. Chin, K. Yamanouchi, Y. Cheng, and Z. Xu, Phys. Rev. X **3**, 041009 (2013).

[3] H. Xu, E. Lötstedt, A. Iwasaki, and K. Yamanouchi, Nat. Commun. **6**, 8347 (2015).

[4] Y. Liu, P. Ding, G. Lambert, A. Houard, V. Tikhonchuk, and A. Mysyrowicz, Phys. Rev. Lett. **115**, 133203 (2015).

[5] J. Yao, S. Jiang, W. Chu, B. Zeng, C. Wu, R. Lu, Z. Li, H. Xie, G. Li, C. Yu, Z. Wang, H. Jiang, Q. Gong, and Y. Cheng, Phys. Rev. Lett. **116**, 143007 (2016).

[6] Y. Liu, P. Ding, N. Ibrakovic, S. Bengtsson, S. Chen, R. Danylo, E. R. Simpson, E. W. Larsen, X. Zhang, Z. Fan, A. Houard,

J. Mauritsson, A. L'Huillier, C. L. Arnold, S. Zhuang, V. Tikhonchuk, and A. Mysyrowicz, Phys. Rev. Lett. **119**, 203205 (2017).
[7] M. Britton, P. Laferrière, D. H. Ko, Z. Li, F. Kong, G. Brown, A. Naumov, C. Zhang, L. Arissian, and P. B. Corkum, Phys. Rev. Lett. **120**, 133208 (2018).
[8] Z. Liu, J. Yao, J. Chen, B. Xu, W. Chu, and Y. Cheng, Phys. Rev. Lett. **120**, 083205 (2018).
[9] H. Li, M. Hou, H. Zang, Y. Fu, E. Lötstedt, T. Ando, A. Iwasaki, K. Yamanouchi, and H. Xu, Phys. Rev. Lett. **122**, 013202 (2019).
[10] T. Ando, E. Lötstedt, A. Iwasaki, H. Li, Y. Fu, S. Wang, H. Xu, and K. Yamanouchi, Phys. Rev. Lett. **123**, 203201 (2019).
[11] A. Mysyrowicz, R. Danylo, A. Houard, V. Tikhonchuk, X. Zhang, Z. Fan, Q. Liang, S. Zhuang, L. Yuan, and Y. Liu, APL Photon. **4**, 110807 (2019).
[12] H. Li, E. Lötstedt, H. Li, Y. Zhou, N. Dong, L. Deng, P. Lu, T. Ando, A. Iwasaki, Y. Fu, S. Wang, J. Wu, K. Yamanouchi, and H. Xu, Phys. Rev. Lett. **125**, 053201 (2020).
[13] C. Kleine, M.-O. Winghart, Z.-Y. Zhang, M. Richter, M. Ekimova, S. Eckert, M. J. J. Vrakking, E. T. J. Nibbering, A. Rouzée, and E. R. Grant, Phys. Rev. Lett. **129**, 123002 (2022).
[14] X. Zhang, R. Danylo, Z. Fan, P. Ding, C. Kou, Q. Liang, A. Houard, V. Tikhonchuk, A. Mysyrowicz, and Y. Liu, Appl. Phys. B **126**, 53 (2020).
[15] M. Lytova, M. Richter, F. Morales, O. Smirnova, M. Ivanov, and M. Spanner, Phys. Rev. A **102**, 013111 (2020).
[16] M. Richter, M. Lytova, F. Morales, S. Haessler, O. Smirnova, M. Spanner, and M. Ivanov, Optica **7**, 586 (2020).
[17] V. T. Tikhonchuk, Y. Liu, R. Danylo, A. Houard, and A. Mysyrowicz, New J. Phys. **23**, 023035 (2021).
[18] V. T. Tikhonchuk, Y. Liu, R. Danylo, A. Houard, and A. Mysyrowicz, Phys. Rev. A **104**, 063116 (2021).
[19] Z. Li, B. Zeng, W. Chu, H. Xie, J. Yao, G. Li, L. Qiao, Z. Wang, and Y. Cheng, Sci. Rep. **6**, 21504 (2016).
[20] G. Li, C. Jing, B. Zeng, H. Xie, J. Yao, W. Chu, J. Ni, H. Zhang, H. Xu, Y. Cheng, and Z. Xu, Phys. Rev. A **89**, 033833 (2014).
[21] H. Zhang, C. Jing, G. Li, H. Xie, J. Yao, B. Zeng, W. Chu, J. Ni, H. Xu, and Y. Cheng, Phys. Rev. A **88**, 063417 (2013).
[22] Y. Wan, B. Xu, J. Yao, J. Chen, Z. Liu, F. Zhang, W. Chu, and Y. Cheng, J. Opt. Soc. Am. B **36**, G57 (2019).
[23] Y. Fu, E. Lötstedt, H. Li, S. Wang, D. Yao, T. Ando, A. Iwasaki, F. H. M. Faisal, K. Yamanouchi, and H. Xu, Phys. Rev. Res. **2**, 012007(R) (2020).
[24] P. Ding, Lasing effect in femtosecond filaments in air, Thesis, Université Paris Saclay (COmUE), 2016.
[25] S. Rostami, J.-C. Diels, and L. Arissian, Opt. Express **23**, 3299 (2015).
[26] X. M. Tong, Z. X. Zhao, and C. D. Lin, Phys. Rev. A **66**, 033402 (2002).
[27] S. Xue, S. Yue, H. Du, B. Hu, and A.-T. Le, Phys. Rev. A **104**, 013101 (2021).
[28] S. Xue, S. Sun, P. Ding, B. Hu, S. Yue, and H. Du, Phys. Rev. A **105**, 043108 (2022).
[29] Y. R. Liu, Y. Wu, J. G. Wang, O. Vendrell, V. Kimberg, and S. B. Zhang, Phys. Rev. A **102**, 033114 (2020).
[30] S. Pabst, M. Lein, and H. J. Wörner, Phys. Rev. A **93**, 023412 (2016).
[31] L. Xu, Q. Lu, V. T. Tikhonchuk, B. Zhou, R. Yang, Q. Liang, F. He, R. Danylo, A. Houard, A. Mysyrowicz, and Y. Liu, Opt. Express **30**, 38481 (2022).
[32] Q. Zhang, H. Xie, G. Li, X. Wang, H. Lei, J. Zhao, Z. Chen, J. Yao, Y. Cheng, and Z. Zhao, Commun. Phys. **3**, 50 (2020).
[33] H. Xie, H. Lei, G. Li, J. Yao, Q. Zhang, X. Wang, J. Zhao, Z. Chen, Y. Cheng, and Z. Zhao, Photon. Res. **9**, 2046 (2021).
[34] H. Xie, H. Lei, G. Li, Q. Zhang, X. Wang, J. Zhao, Z. Chen, J. Yao, Y. Cheng, and Z. Zhao, Phys. Rev. Res. **2**, 023329 (2020).
[35] H. Lei, G. Li, H. Xie, Q. Zhang, X. Wang, J. Zhao, Z. Chen, and Z. Zhao, Opt. Express **28**, 22829 (2020).
[36] A. A. Svidzinsky, L. Yuan, and M. O. Scully, New J. Phys. **15**, 053044 (2013).
[37] H. Li, Q. Song, J. Yao, Z. Liu, J. Chen, B. Xu, K. Lin, J. Qiang, B. He, H. Xu *et al.*, Phys. Rev. A **99**, 053413 (2019).
[38] Y. Zhang, Z. Zhu, Y. Zheng, Y. Wu, Y. He, Z. Cui, B. Hu, P. Ding, and J. Ding, Phys. Rev. A **103**, 063110 (2021).